Geometric Integration of Heterogeneous Models for Multisatellite Image Positioning

Liang-Chien Chen, Wen-Chi Chang, and Tee-Ann Teo

***Abstract*—With the wider availability of more and more images acquired from various satellites, the integration of different orientation models for different sensors has become an important task in order to maintain geometrical consistency. This study combines two heterogeneous geometric correction models, namely, direct georeferencing and the rational function model for multisatellite image positioning. Two types of adjustment models, collocation-based block adjustment (CBBA) and collocation-aided block adjustment (CABA), are proposed to reach the goal. The former is based on the concept that the adjustment is first performed on individual images, and then, all images are integrated. Discrepancies are compensated for by least squares collocation (LSC). The latter method entails simultaneous adjustment of the two heterogeneous models followed by LSC. Experimental results indicate that the proposed method can significantly improve the geometric accuracy as well as reduce geometric discrepancies between images. We also demonstrate that CABA is slightly better than CBBA.**

***Index Terms*—Direct georeferencing (DG), least squares collocation (LSC), rational function model (RFM).**

I. Introduction

With the improvement of satellite technology, satellite imagery has become a common and important data source for GIS applications. Such data sets, however, usually contain multitemporal or multisensor images, which need registration and mosaicking. To insure the quality of the registration and mosaicking, a block adjustment that can take into account different candidate images produced with different mathematical models is needed.

Block adjustment strategies for satellite images include the rigorous sensor model (RSM) [1] and rational function model (RFM) [2]–[6]. RSM describes the relationship of a ground point with respect to its image counterpart and exterior orientation parameters (EOPs). RFM uses the rational polynomial coefficients (RPCs) to transform object coordinates into the image space. Thus, parameters treated during the process of block adjustment for these two models are different. In fact, the availability of these parameters is satellite dependent. Some satellite companies provide RPCs instead of EOPs, others the opposite. Thus, for heterogeneous models between RSM and RFM, one needs to combine and integrate these two types of images for block adjustment.

There are two methods for RSM, namely, bundle adjustment [7]–[10] and direct georeferencing (DG) [11]–[13]. Bundle adjustment simultaneously builds up the collinearity condition for all image points with respect to the object points; coherent ground control points (GCPs) are to some degree fixed. DG employs the recorded dynamic orientation parameters to establish an observation vector for each image point followed by a fitting procedure using GCPs. The treated orientation parameters are obtained from GPS, IMU, and star trackers. Popularly used in photogrammetry, the bundle adjustment method takes advantage of favorable convergence geometry. Thus, the suitability of the initial values for the orientation parameters might not be so important. On the other hand, if the orientation observations, including orbital and attitude data, are accurate, the DG is a good alternative. Taking advantage of good EOPs, the DG approach derives favorable results for satellite images with fewer GCPs than are needed for bundle adjustment. We thus combine the DG of RSM with RFM in this investigation.

During block adjustment, it is necessary to combine all images so as to maintain consistency of the geometrical registration [14], [15]. The simultaneous approach for combined adjustment is to build a mathematical model that contains two heterogeneous geometric models. The treated parameters for satellites, including the EOPs and RPCs, have recently become precise enough so that adjustment on a single-image basis might also reach high enough accuracy for geometric correction.

It is known that the attitude of a satellite image may include high-frequency variations that are not easy to account for when smooth functions, for instance, polynomials, are selected in the DG approach for RFM generation. Thus, local systematic errors may remain. In this investigation, the traditional approach, i.e., geometrical fitting, followed by a fine-tuning procedure is used. Nonlinear components in the fine-tuning procedure are indicative of possible local systematic errors. Least squares collocation (LSC) is a geostatistical method [16], which can extract local signals after regression. Thus, LSC is selected as the approach for compensation for local systematic errors. There are two possible ways to include LSC in the adjustment for orientation modeling. The first one is based on the spatial resection of individual images, after which the residuals of the reference points, which includes the GCPs and the tie points (TPs), are employed for the LSC. The second approach typically includes the LSC for simultaneous block adjustment of images with heterogeneous orbit parameters. Since the first method relies on LSC to connect images, it is called collocation-based block adjustment (CBBA). The role of

Manuscript received May 7, 2010; revised June 1, 2011 and October 1, 2011; accepted October 8, 2011. Date of publication December 26, 2011; date of current version June 20, 2012.

L.-C. Chen and W.-C. Chang are with the Digital Photogrammetry Laboratory, Center for Space and Remote Sensing Research, National Central University, Jhongli City 32001, Taiwan (e-mail: lcchen@csrsr.ncu.edu.tw; wenchi@csrsr.ncu.edu.tw).

T.-A. Teo is with the Department of Civil Engineering, National Chiao Tung University, Hsinchu 30010, Taiwan (e-mail: tateo@mail.nctu.edu.tw).

Color versions of one or more of the figures in this paper are available online at http://ieeexplore.ieee.org.

Digital Object Identifier 10.1109/TGRS.2011.2176739

0196-2892/$26.00 © 2011 IEEE

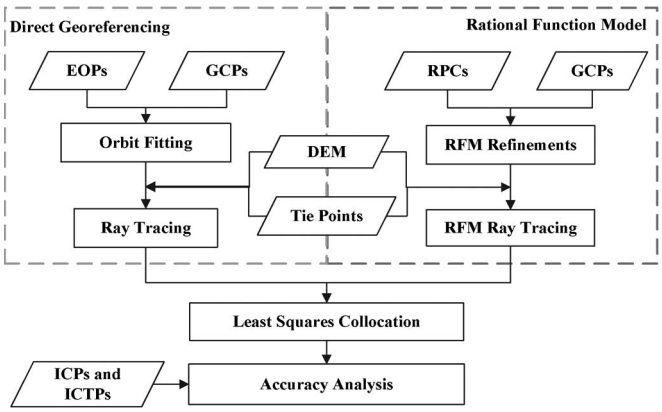

Fig. 1. Work flow of CBBA.

LSC in the second approach is simply to fine-tune the results for simultaneous adjustment; thus, we call it collocation-aided block adjustment (CABA).

It is observed that the major applications for remotely sensed images are for the detection of natural resources and land cover monitoring. In order to acquire the largest possible coverage, the area of image overlap should be small. However, satellite imaging systems usually have a small field of view. Thus, the convergence geometry is generally not favorable. Weak geometry at the intersection may cause large elevation errors that could affect the adjustment [17]. To avoid such problems, this study will employ digital elevation models (DEMs) for elevation control. Thus, both the proposed methods, namely, the CBBA and CABA adjustment models, will be tested using DEMs as the elevation control for multisatellite image positioning in this investigation.

After the motives of this study, CBBA and CABA models are introduced in detail in the second section. Next, we report experiments with multisatellite images. The final section is the conclusions.

II. Proposed Scheme

The proposed scheme is composed of two adjustment models, i.e., CBBA and CABA. The details of each model are given next.

A. CBBA

CBBA includes three major parts. First, the DG mathematics related to orbital fitting and ray tracing are built. Second, the RFM is set up by refining RFM and RFM ray tracing. Both of these parts are about single-image adjustment. Treatment by LSC of discrepancies between images is still needed to compensate for the object coordinates. A flowchart of the CBBA work process is shown in Fig. 1.

The DG mathematical equation is shown in (1) in the geocentric coordinate system. The $x(t_i), y(t_i), z(t_i)$, and u_{Xi}, u_{Yi}, u_{Zi} are derived from the EOPs. Systematic errors that exist in the EOPs must be compensated for using GCPs through orbital fitting. The DG equation for the orbital fitting process is shown in (2). Considering the extremely high correlation between the orbital parameters and attitude data, only the orbital position is corrected during fitting. Furthermore, the slight residues are corrected by LSC. The remaining errors, which are small, are taken care of by the LSC.

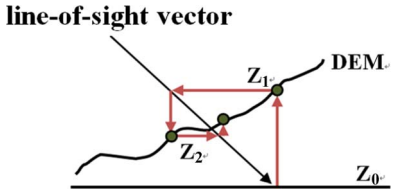

Fig. 2. Illustration of ray tracing.

$$\begin{aligned} X_i &= x(t_i) + S_i u_{Xi} \\ Y_i &= y(t_i) + S_i u_{Yi} \\ Z_i &= z(t_i) + S_i u_{Zi} \end{aligned} \tag{1}$$

$$\begin{aligned} X_i &= x_0 + a_0 + a_1 t + S_i u_{Xi} \\ Y_i &= y_0 + b_0 + b_1 t + S_i u_{Yi} \\ Z_i &= z_0 + c_0 + c_1 t + S_i u_{Zi} \end{aligned} \tag{2}$$

where

X_i, Y_i, Z_i	ground points;
$x(t_i), y(t_i), z(t_i)$	satellite positions;
u_{Xi}, u_{Yi}, u_{Zi}	satellite line-of-sight vectors;
S_i	scaling factor;
t_i	time;
x_0, y_0, z_0	satellite positions obtained from EOPs;
$a_0, a_1, b_0, b_1, c_0, c_1$	orbital correction parameters.

After orbital fitting, the line-of-sight vector of the image coordinates can be calculated by ray tracing [7]. The tracing procedure is used to locate the object position for an image point, provided that the EOPs and the DEMs are available. The purposes of ray tracing are twofold: to obtain the object coordinates for all points and to calculate the residues for LSC. In addition, the elevation control may be integrated by employing DEMs to cope with the weak convergent geometry of the images. The planimetric coordinates of the object space for the GCPs can be obtained through the intersection of the line-of-sight vectors and the known elevation. For a tie point, an initial elevation is needed for ray tracing. The planimetric coordinates of the object space can be obtained from the line-of-sight vectors and initial elevation. The new elevation, which is generated by interpolating the DEMs, is derived to replace the initial elevation. The new elevation is used as an initial value in the next iteration. This step is repeated until the difference between the new elevation and the initial value is small enough. An illustration of the ray tracing method is shown in Fig. 2.

RFM uses the ratio of two polynomials to build the relationship between the object space and the image space, formulated as in

$$s = \frac{\sum_{i=0}^{m1}\sum_{j=0}^{m2}\sum_{k=0}^{m3} c_{ijk}\varphi^i\lambda^j h^k}{\sum_{i=0}^{n1}\sum_{j=0}^{n2}\sum_{k=0}^{n3} d_{ijk}\varphi^i\lambda^j h^k} \quad l = \frac{\sum_{i=0}^{m1}\sum_{j=0}^{m2}\sum_{k=0}^{m3} e_{ijk}\varphi^i\lambda^j h^k}{\sum_{i=0}^{n1}\sum_{j=0}^{n2}\sum_{k=0}^{n3} f_{ijk}\varphi^i\lambda^j h^k} \tag{3}$$

where

s, l	image coordinates;
φ, λ, h	object coordinates in the geographic coordinate system;
$c_{ijk}, d_{ijk}, e_{ijk}, f_{ijk}$	RPCs.

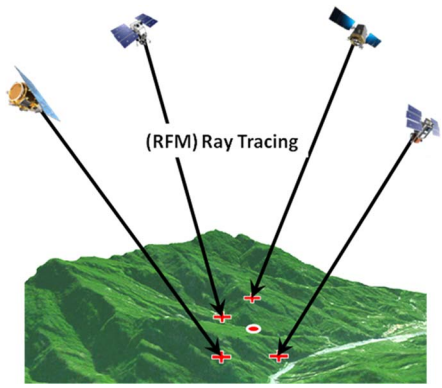

Fig. 3. Illustration of relative discrepancy.

As suggested by previous studies [18], the third degree polynomial is selected in the RFM. In this case, it contains 80 RPCs.

Since the RPCs are derived from ephemeris data that include errors in orbital parameters and attitude data, we need to refine the RFM. RFM refinement starts from the object space. The object coordinates are mapped to the RFM image space via RPCs. The affine transformation parameters are then calculated from the GCP image coordinates and the GCP RFM image coordinates. The systematic bias of the RPCs is compensated for by affine transformation [19]. The equation for RFM refinement is

$$\begin{aligned} S_{\mathrm{GCP}} &= A_0 + A_1 \cdot S_{\mathrm{RFM}} + A_2 \cdot L_{\mathrm{RFM}} \\ L_{\mathrm{GCP}} &= B_0 + B_1 \cdot S_{\mathrm{RFM}} + B_2 \cdot L_{\mathrm{RFM}} \end{aligned} \tag{4}$$

where

$S_{\mathrm{GCP}}, L_{\mathrm{GCP}}$ image coordinates of the GCP;
$S_{\mathrm{RFM}}, L_{\mathrm{RFM}}$ image coordinates determined by RFM;
$A_0 \sim B_2$ affine coefficients.

Similar to DG, the next step is to calculate the 3-D object coordinates and the residuals after RFM refinement. RFM ray tracing is employed for this purpose. The procedure is conceptually identical to ray tracing, except that the mathematics used are RFM functions. Given the image coordinates of a point, an initial elevation h_0 is employed to calculate the corresponding φ_0 and λ_0. Then, the new elevation is replaced according to the position in the DEMs. This step is repeated until the difference is small enough.

Once the correct parameters have been obtained for each image, including the DG orbital correction parameters and the RFM affine coefficients, discrepancies among those images can be estimated through the bias of object coordinates determined by the DG or the RFM. The bias of the GCPs is obtained by differencing the object coordinates obtained from ray tracing (RFM ray tracing) and the reference coordinates. The TP residues are defined using the relative discrepancy. Fig. 3 shows an example of determining the relative discrepancy. A set of TPs exists for four images. Four object coordinates can be obtained from ray tracing or RFM ray tracing. Then, the weighted average position is calculated with these object coordinates. Since we assume that the positioning error is proportional to image resolution, it might be reasonable to estimate the positioning variance to be the square of ground sampling distance (GSD). Thus, we select the weight for each image point inversely proportional to its GSD. The equations for the weighted average position are shown in

$$\begin{aligned} X &= \sum_{n=1}^{n=m} \frac{X_n}{GSD_n^2} \Big/ \sum_{n=1}^{n=m} \frac{1}{GSD_n^2} \\ Y &= \sum_{n=1}^{n=m} \frac{Y_n}{GSD_n^2} \Big/ \sum_{n=1}^{n=m} \frac{1}{GSD_n^2} \\ Z &= \sum_{n=1}^{n=m} \frac{Z_n}{GSD_n^2} \Big/ \sum_{n=1}^{n=m} \frac{1}{GSD_n^2} \end{aligned} \tag{5}$$

where

X, Y, Z weighted average positions;
X_n, Y_n, Z_n object coordinates obtained from ray tracing or RFM ray tracing;
m number of images.

The relative discrepancy is thus the distance between the corresponding object coordinate and the weighted average position.

In (6), the LSC method is employed to compensate for the relative discrepancy among these images. The covariance matrices σ_k and Σ_k used in this study include the geostatistical characteristics among a group of points in terms of self-correlation and cross-correlation. To determine each element of the covariance matrix in σ_k and Σ_k, a Gaussian function C is selected for the covariance function [20] as shown in (7). In this paper, the reference points include GCPs and TPs.

$$\rho_k = \sigma_k \cdot [\Sigma_k]^{-1} \cdot v_k \tag{6}$$

where

k x-, y-, and z-axes;
ρ_k correction of the interpolated point;
σ_k row covariance matrix for the interpolated point with respect to the reference points;
Σ_k covariance matrix for the reference points;
v_k residual vectors for the reference points.

$$C = \begin{cases} (1 - r_n)\mu_k \exp^{-\left(2.146 \frac{d}{d_{\max}}\right)^2}, & \text{if } d \neq 0 \\ \mu_k, & \text{if } d = 0 \end{cases} \tag{7}$$

where

C element in the covariance matrices of σ_k and Σ_k;
d 3-D distance between the interpolation point and the reference points;
$d_{\max}$ maximum 3-D distance in the collocation;
μ_k variance of the reference points' residuals;
r_n filtering ratio (we use 0.1 in the experiment);
2.146 selected so that the covariance limit is $1\% * (1 - r_n)\mu_k$ when $d = d_{\max}$.

B. CABA

The CABA method is composed of two major parts. The first part considers the global geometry, including elevation control, absolute accuracy, and the discrepancy among all employed images, through the process of block adjustment, which is built using DG and RFM mathematical equations. LSC aids in compensating for any local systematic errors that may still exist after block adjustment. Fig. 4 shows the work flow of CABA.

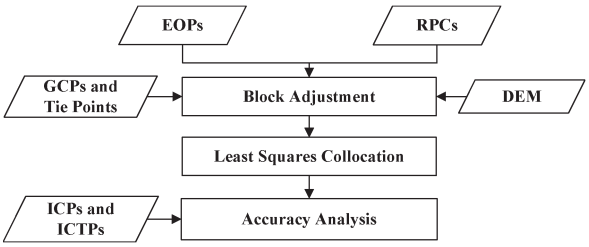

Fig. 4. Work flow of CABA.

Three types of observation equations are contained in the block adjustment process: the DG observation equations, the RFM observation equations, and the pseudoequations for ground coordinates.

The DG equation with orbital fitting is shown in (2). The unknown values in this equation include the ground points, the scaling factor, and the orbital correction parameters. In order to reduce the unknown values, the DG observation equation is arranged as in (8). Therefore, the scaling factor can be removed. After linearization, the least squares form of the DG observation equation is represented in a matrix form as in (9). It should be noted that the DG is in the geocentric coordinate system. However, the RFM is in the geographic coordinate system. In order to integrate the two models, the working coordinate system should be unified. The geographic coordinate system (φ, λ, h) is selected as the working coordinate system in this study.

$$\begin{aligned} D_1 &= v_{xi} = (x_0 + a_0 + a_1 \cdot t - X_i)/(z_0 + c_0 + c_1 \cdot t - Z_i) \\ &\quad - u_{Xi}/u_{Zi} \\ D_2 &= v_{yi} = (y_0 + b_0 + b_1 \cdot t - Y_i)/(z_0 + c_0 + c_1 \cdot t - Z_i) \\ &\quad - u_{Yi}/u_{Zi} \end{aligned} \tag{8}$$

$$\begin{bmatrix} v_{xi} \\ v_{yi} \end{bmatrix} = \begin{bmatrix} \frac{\partial D_1}{\partial a_0} & \frac{\partial D_1}{\partial a_1} & 0 & 0 & \frac{\partial D_1}{\partial c_0} & \frac{\partial D_1}{\partial c_1} \\ 0 & 0 & \frac{\partial D_2}{\partial b_0} & \frac{\partial D_2}{\partial b_1} & \frac{\partial D_2}{\partial c_0} & \frac{\partial D_2}{\partial c_1} \end{bmatrix} \begin{bmatrix} da_0 \\ da_1 \\ db_0 \\ db_1 \\ dc_0 \\ dc_1 \end{bmatrix} + \begin{bmatrix} \frac{\partial D_1}{\partial \varphi_i} & \frac{\partial D_1}{\partial \lambda_i} & \frac{\partial D_2}{\partial \varphi_i} \\ \frac{\partial D_2}{\partial \lambda_i} & \frac{\partial D_1}{\partial h_i} & \frac{\partial D_2}{\partial h_i} \end{bmatrix} \begin{bmatrix} d\varphi_i \\ d\lambda_i \\ dh_i \end{bmatrix} - \begin{bmatrix} -D_1^0 \\ -D_2^0 \end{bmatrix} \tag{9}$$

where

D_1, D_2	DG observation equations;
v_{xi}, v_{yi}	residual values for the DG observation equations;
X_i, Y_i, Z_i	ground coordinates in the geocentric coordinate system;
$(\partial D_i/\partial a_0) \sim (\partial D_i/\partial h_i)$	partial derivatives in the linearization.

The treated parameters in the RFM are the affine coefficients. The RFM observation equation is shown in (10). The least squares form of the RFM observation equation can be represented in a matrix form as in (11).

$$\begin{aligned} R_1 &= v_{si} = A_0 + A_1 \cdot s_{\mathrm{rfm}} + A_2 \cdot l_{\mathrm{rfm}} - s_{\mathrm{gcp}} \\ R_2 &= v_{li} = B_0 + B_1 \cdot s_{\mathrm{rfm}} + B_2 \cdot l_{\mathrm{rfm}} - l_{\mathrm{gcp}} \end{aligned} \tag{10}$$

$$\begin{bmatrix} v_{si} \\ v_{li} \end{bmatrix} = \begin{bmatrix} \frac{\partial R_1}{\partial A_0} & \frac{\partial R_1}{\partial A_1} & \frac{\partial R_1}{\partial A_2} & 0 & 0 & 0 \\ 0 & 0 & 0 & \frac{\partial R_2}{\partial B_0} & \frac{\partial R_2}{\partial B_1} & \frac{\partial R_2}{\partial B_2} \end{bmatrix} \begin{bmatrix} dA_0 \\ dA_1 \\ dA_2 \\ dB_0 \\ dB_1 \\ dB_2 \end{bmatrix} + \begin{bmatrix} \frac{\partial R_1}{\partial \varphi_i} & \frac{\partial R_1}{\partial \lambda_i} & \frac{\partial R_2}{\partial \varphi_i} \\ \frac{\partial R_2}{\partial \lambda_i} & \frac{\partial R_1}{\partial h_i} & \frac{\partial R_2}{\partial h_i} \end{bmatrix} \begin{bmatrix} d\varphi_i \\ d\lambda_i \\ dh_i \end{bmatrix} - \begin{bmatrix} -R_1^0 \\ -R_2^0 \end{bmatrix} \tag{11}$$

where

R_1, R_2	RFM observation equations;
v_{si}, v_{li}	residual values for the RFM observation equations;
$(\partial R_i/\partial A_0) \sim (\partial R_i/\partial h_i)$	partial derivatives in the linearization.

The pseudoequation for ground coordinates is formulated as shown in (12). It contains GCP ground coordinates and TP ground coordinates. The approximation values for TPs are determined from ray tracing or RFM ray tracing. In this paper, the measured ground coordinate value for a set of TPs is defined by the weighted average position, as shown in Fig. 3.

$$\begin{bmatrix} v_{\varphi_i} \\ v_{\lambda_i} \\ v_{h_i} \end{bmatrix} - \begin{bmatrix} d\varphi_i \\ d\lambda_i \\ dh_i \end{bmatrix} = \begin{bmatrix} \varphi_i^0 - \varphi_i^{00} \\ \lambda_i^0 - \lambda_i^{00} \\ h_i^0 - h_i^{00} \end{bmatrix} \tag{12}$$

where

$v_{\varphi_i}, v_{\lambda_i}, v_{h_i}$	residual values for the pseudoequations for ground coordinates;
$\varphi^0, \lambda^0, h^0$	approximation values of ground coordinates;
$\varphi^{00}, \lambda^{00}, h^{00}$	measured values of ground coordinates.

Following the common notation in block adjustment for aerial images [21], (9), (11), and (12) are combined to obtain

$$\begin{aligned} V_D &= \dot{B}_D \dot{\Delta}_D + \ddot{B}_D \ddot{\Delta}_G - \varepsilon_D \\ V_R &= \dot{B}_R \dot{\Delta}_R + \ddot{B}_R \ddot{\Delta}_G - \varepsilon_R \\ V_G &= (-1)\ddot{\Delta}_G - \varepsilon_G \end{aligned} \tag{13}$$

where

V_D	residual matrix for the DG equation;
$\dot{B}_D, \ddot{B}_D$	observation matrices for the DG equations;
$\dot{\Delta}_D$	matrix of unknown corrections of orbital correction parameters;
V_R	residual matrix for the RFM equation;
$\dot{B}_R, \ddot{B}_R$	observation matrices for the RFM equations;
$\dot{\Delta}_R$	matrix of unknown corrections of affine coefficients;
V_G	residual matrix for the pseudoequation for the ground coordinate equation;
$\ddot{\Delta}_G$	matrix of unknown corrections of the ground coordinates;
$\varepsilon_D, \varepsilon_R, \varepsilon_G$	approximation matrices of measurements.

A simpler form of the whole observation equations is shown in (14). The weighting matrix is shown in (15). The weight is composed of the DG equation, the RFM equation and the ground coordinates. The orbital correction parameters for DG, the affine coefficients for RFM, and the ground coordinates for

GCPs and TPs can be determined with the least squares method after the observation equations have been completed.

$$\overline{V} = \overline{B}\Delta - \overline{C} \tag{14}$$

$$W = \begin{bmatrix} W_D & 0 & 0 \\ 0 & W_R & 0 \\ 0 & 0 & W_G \end{bmatrix} \tag{15}$$

where

$\overline{V}$ residual matrix;
$\overline{B}$ observation matrix for the equations;
Δ matrix of unknown parameters;
$\overline{C}$ approximation matrix of measurements;
W_D weight of the DG observation equations;
W_R weight of the RFM observation equations;
W_G weight of the ground coordinates.

The orbital correction parameters for DG, the affine coefficients for RFM, and the ground coordinates for GCPs and TPs can be determined with the least squares method after the observation equations have been completed. The next step is LSC in order to compensate for the local systematic error. The details of LSC have been given in the previous section.

C. Accuracy Analysis

The analyzed items include the absolute accuracy and the geometrical consistency between images. We use independent check points (ICPs) and independent check tie points (ICTPs) with the proposed model to evaluate the absolute accuracy and the geometrical consistency between images, respectively. The bias between the determined object coordinates and the true coordinates is calculated so as to find the root-mean-squared error (rmse) for the ICPs. The ICTPs' rmse is obtained from the relative discrepancy for each image.

III. Experimental Results

The experiments include three cases. Case I tests images with a 2-m/2.5-m resolution. Case II tests images with submeter resolution. Case III is for multiresolution images. The performance of the single-image adjustment, CBBA, and CABA is compared. The validation takes into consideration the absolute accuracy and geometric consistency between images.

The data set for Case I contains SPOT-5, Formosat-2, and ALOS satellite images. DG is used for the geometric correction of SPOT-5 and Formosat-2 satellite images. RFM is used for ALOS satellite image. GCPs and ICPs are obtained from 1:5000 scaled topographic maps. The GCP accuracy is estimated to be better than 3 m. The TPs and ICTPs are acquired by manual measurements. Information related to the test images is given in Table I. Fig. 5 shows the test images and the overlapping area between those images.

For Case II, the high-resolution images include WorldView-1, QuickBird, and Geoeye-1 images. The GSDs are submeter for these images. The GCPs and ICPS for Case II and Case III were obtained from the GCP database of the Ministry of the Interior, Taiwan, through manual measurements. The measurement accuracy is estimated to be better than 0.5 m. The related information is shown in Table II. Fig. 6 shows the test images and the overlapping area of those images.

TABLE I
Information Related to Test Data for Case I

Descriptions	SPOT-5	Formosat-2	ALOS
Geometric Model	RSM	RSM	RFM
Level	1A	1A	1A
Date	2008/8/26	2008/5/18	2008/4/22
GSD (m)	2.61	2.02	2.50
Viewing Angle (degree)	12.3	6.2	-1.4
Image Size	24000 x 24000	12000 x 12000	19872 x 16000
No. of GCPs/ICPs	27/53	9/21	9/21
No. of TPs/ICTPs	25/47		
DEM	40m Topographic Data Base of Taiwan		

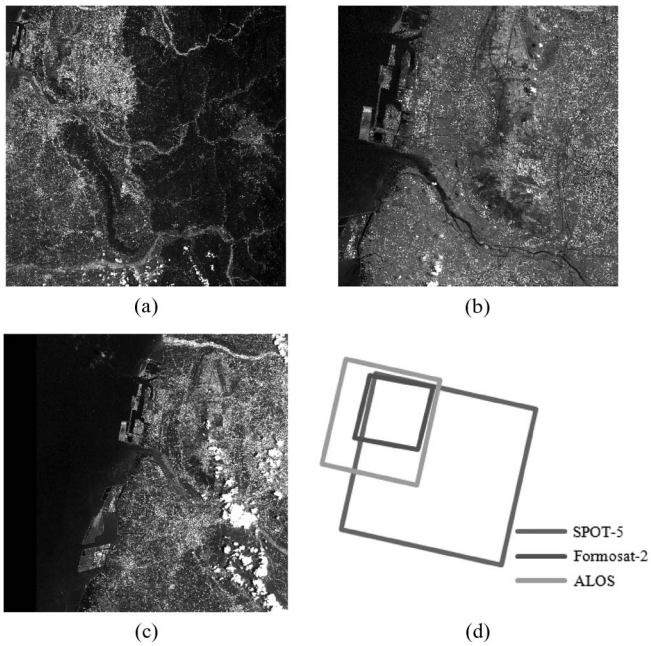

Fig. 5. Test images for Case I and the overlapping area. (a) SPOT-5 CNES, 2008. (b) Formosat-2 NSPO, 2008. (c) ALOS JAXA, 2008.

TABLE II
Information Related to Test Data for Case II and Case III

Descriptions	WorldView-1	QuickBird	Geoeye-1
Geometric Model	RFM	RSM	RFM
Level	Basic	Basic	Standard
Date	2007/11/25	2005/12/23	2009/9/20
GSD (m)	0.67	0.63	0.5
Elevation (degree)	52.6	76.9	70.96
Azimuth (degree)	26.9	117.7	123.89
Image Size	35170 x 23708	27552 x 29320	19872 x 16000
No. of GCPs/ICPs	9/31	9/20	5/6
No. of TPs/ICTPs	16/24	16/24	16/21
DEM	5m Topographic Data Base of Taiwan		

Case III tests the multiresolution images. The test data integrate WorldView-1, QuickBird, Geoeye-1, Kompsat-2, and two Formosat-2 satellite images. The first three images are the same as those used in Case II. Information related to the Kompsat-2 and two Formosat-2 satellite images is given in Table III. Fig. 7 shows the three images and the overlapping area between the six images.

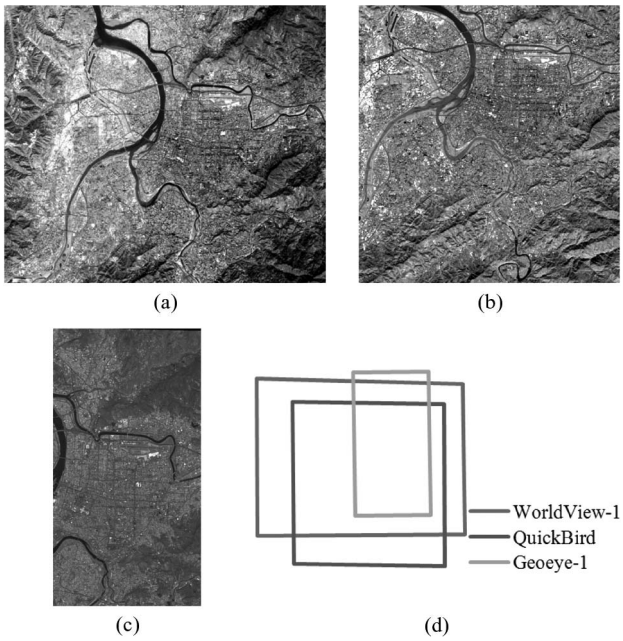

Fig. 6. Test images in Case II and Case III and the overlapping area. (a) WorldView-1 DigitalGlobe, 2007. (b) QuickBird DigitalGlobe, 2005. (c) Geoeye-1 Geoeye, 2009. (d) Overlapping area.

TABLE III
INFORMATION RELATED TO TEST DATA FOR CASE III

Descriptions	Kompsat-2	Formosat-2_1	Formosat-2_2
Geometric Model	RFM	RSM	RSM
Level	1A	1A	1A
Date	2007/10/21	2006/8/19	2007/1/30
GSD (m)	1.03	2.01	2.45
Viewing Angle (degree)	-11.26	3.93	25.47
Image Size	15000 x 15500	12000 x 12000	12000 x 12000
No. of GCPs/ICPs	5/12	9/18	9/22
No. of TPs/ICTPs	11/20	6/17	6/14
DEM	5m Topographic Data Base of Taiwan		

The experiment compares the results of **CBBA**, **CABA**, and single-image adjustment. To reveal the contributions of LSC, the results of single-image adjustment without collocation, herein named **single**, are also given. The Formosat-2, WorldView-1, Quickbird, Geoeye-1, and Kompsat-2 satellites images are labeled **FS**, **WV**, **QB**, **GE**, and **KP**, respectively, in those results.

A. Case I—Similar Resolution Images (Lower Resolution)

1) Absolute Accuracy: The absolute accuracy is evaluated through ICPs. The histogram of the rmse for ICPs is shown in Fig. 8. For SPOT-5 and FS images, the CBBA and CABA provided better results in the North and South directions than did the single-image adjustment process. The improvement was about 1 and 0.25 m for SPOT-5 and FS, respectively. However, the accuracy decreased by about 0.5 m for the ALOS image. The poor performance of the ALOS case in terms of the absolute accuracy might be due to the unfavorable distribution of GCPs. According to Fig. 8, there are insignificant differences between the CBBA and CABA methods in this case. The

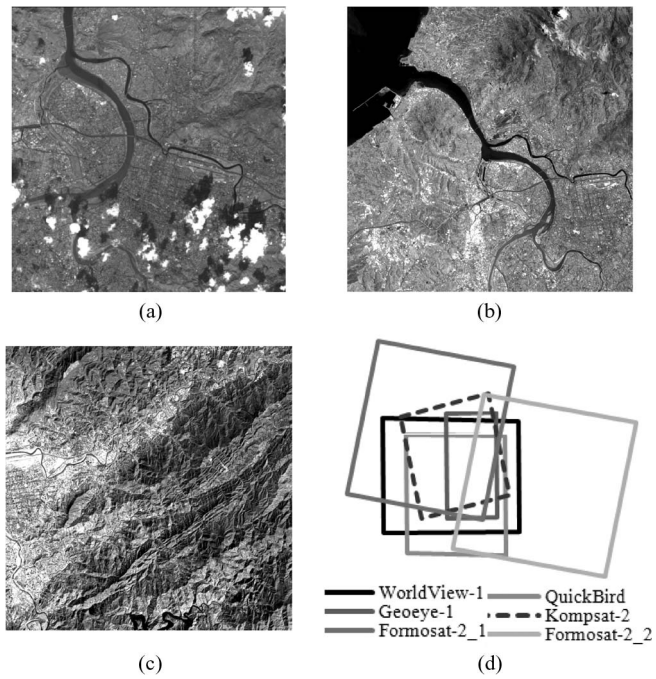

Fig. 7. Test images for Case III and the overlapping area. (a) Kompsat-2 KARI, 2007. (b) Formosat-2_1 NSPO, 2006. (c) Formosat-2_2 NSPO, 2007. (d) Overlapping area.

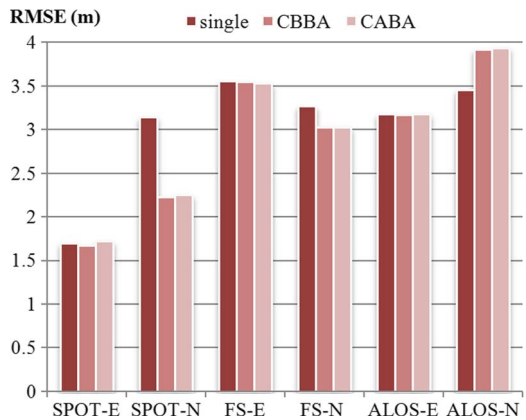

Fig. 8. RMSE of ICPs for Case I.

absolute accuracy is nearly 2 m for SPOT. The FS and ALOS are 3.5 and 4 m, respectively.

2) Geometrical Consistency Between Images: The geometrical consistency between images is examined by looking at discrepancies in the ICTPs. The results are shown in Fig. 9. The discrepancies are better than one pixel for all images. The FS is about 2 m. The errors in SPOT-5 and ALOS are less than 2 m. The results also indicate that the CBBA and CABA methods can improve the geometrical consistency between images. The improvement is more than 0.5 m for ALOS in the North and South directions. The differences between CBBA and CABA are also small.

B. Case II—Similar Resolution Images (Higher Resolution)

1) Absolute Accuracy: This case test is for higher resolution images, including WV, QB, and GE images. Fig. 10 shows the

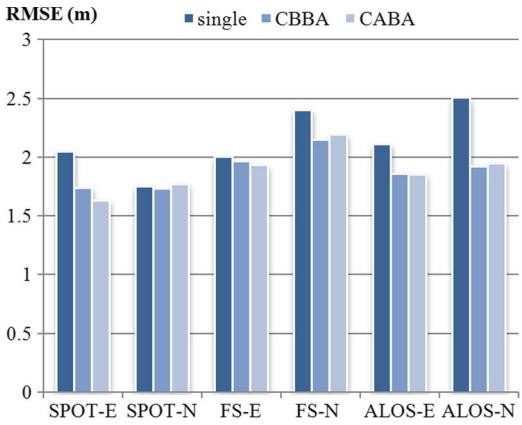

Fig. 9. RMSE of ICTPs for Case I.

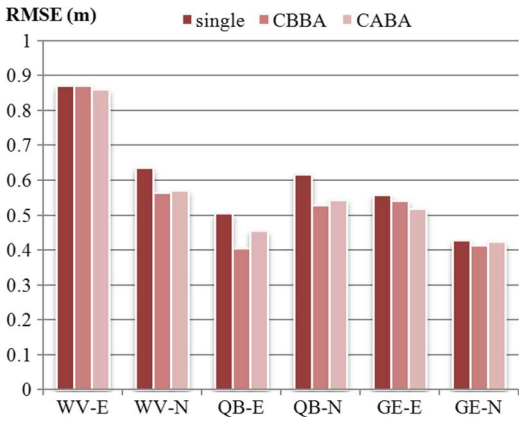

Fig. 10. RMSE of ICPs for Case II.

results of absolute accuracy for Case II. From Fig. 10, it can be seen that the differences obtained with the three methods are insignificant. However, the CBBA and CABA methods are slightly better than the single-image adjustment method. The accuracy for WV in the East and West directions is the worst, about 0.9 m. The accuracy for other images is better than 0.6 m.

2) Geometrical Consistency Between Images: The rmse for discrepancies is shown in Fig. 11. It can be seen that the CBBA and CABA methods offer improved geometrical consistency between images. The accuracy for WV and QB in the North and South directions has increased to more than 0.1 m. The relative discrepancy is less than one pixel for all images. Similarly, the differences between CBBA and CABA are small.

C. Case III—Multiresolution Images

1) Absolute Accuracy: Six images are employed in this case: WV, QB, GE, KP, and two FS images. A histogram of the rmse for the ICPs is shown in Fig. 12. Although CBBA and CABA are insignificantly different in Case I and Case II, the advantage of CABA is obvious in Case III.

The absolute accuracy for WV is about 0.9 m and is better than 0.5 m for the QB and GE images. The absolute accuracy of KP is approximately 2 m. There is still a small difference between the three methods for higher resolution images. The improvements for the two FS images obtained through CBBA are about 2 m in the East and West directions; moreover, the

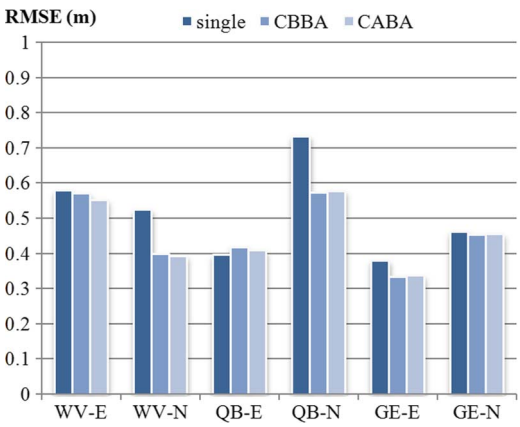

Fig. 11. RMSE of ICTPs for Case II.

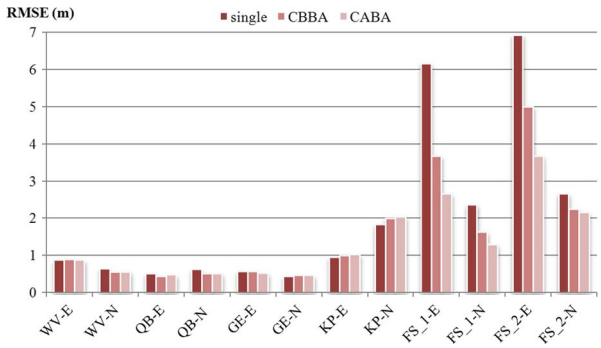

Fig. 12. RMSE of ICPs for Case III.

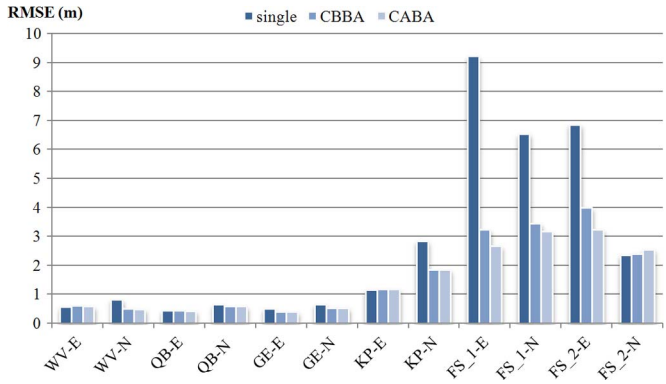

Fig. 13. RMSE of ICTPs for Case III.

accuracy can be improved to about 3.5 m when CABA is employed.

2) Geometrical Consistency Between Images: Fig. 13 shows the geometrical consistency results between images for case III. The CBBA and CABA methods perform slightly better than the single-image adjustment process for the WV, QB, and GE images. The errors are approximately 0.5 m. The relative discrepancy can be improved from about 3 m to less than 2 m. The improvement is significant for the two FS images. The relative discrepancy for the former is about 9 m, with single-image adjustment. This decreases to approximately 3 m using CBBA, and even more through CABA. The results are the same for the second one. The errors obtained are from 7 m to about 4 and 3 m using CBBA and CABA, respectively.

D. Summary of the Experimental Results

The experimental results are summarized as follows.

1) The proposed methods, including CBBA and CABA, improve geometric consistency between images with respect to single-image adjustment. The improvements are more obvious in multiresolution case than in similar resolution cases.
2) The geometrical performances of the CBBA and the CABA are similar when similar resolution images are employed. It is conjectured that, since the treated parameters of satellites are precise enough, and similar in resolution, the differences between CBBA and CABA are insignificant.
3) The CBBA and the CABA offer significant improvement in absolute accuracy and geometric consistency with lower resolution images during the process of single-image adjustment when multiresolution images are used.

CBBA is more straightforward than CABA in terms of the adjustment model. However, the CABA is more generally applicable.

IV. Conclusion

In this paper, we have proposed two approaches to block adjustment for multisensor satellite images, namely, CBBA and CABA. The experimental results indicate that the proposed methods can significantly improve the geometrical accuracy as well as reduce discrepancies when multiresolution images are used. Tests indicate that the proposed methods should be feasible for real applications. Although the differences between CBBA and CABA are insignificant when the resolutions of the images are similar, CABA performs better in multiresolution tests.

References

[1] D. Poli, L. Zhang, and A. Gruen, "Orientation of satellite and airborne imagery from multi-line pushbroom sensors with a rigorous sensor model," *Int. Arch. Photogramm. Remote Sens.*, vol. 35, no. B1, pp. 130–135, 2004.

[2] C. S. Fraser, G. Dial, and J. Grodecki, "Sensor orientation via RPCs," *ISPRS J. Photogramm. Remote Sens.*, vol. 60, no. 3, pp. 182–194, May 2006.

[3] K. Jacobsen, "Geometric modelling of linear CCDs and panoramic imagers," in *Advances in Photogrammetry, Remote Sensing and Spatial Information Science: 2008 ISPRS Congress Book*. New York: Taylor & Francis, 2008, pp. 145–155.

[4] C. V. Tao and Y. Hu, "3D reconstruction methods based on the rational function model," *Photogramm. Eng. Remote Sens*, vol. 68, no. 7, pp. 705–714, Jul. 2002.

[5] N. Mayumi, C. S. Fraser, N. Takayuki, S. Takahiro, and O. Shoichi, "Accuracy assessment of QuickBird stereo imagery," *Photogramm. Rec.*, vol. 19, no. 106, pp. 128–137, Jun. 2004.

[6] J. Grodecki and G. Dial, "Block adjustment of high-resolution satellite image described by rational function," *Photogramm. Eng. Remote Sens.*, vol. 69, no. 1, pp. 59–68, Jan. 2003.

[7] L. C. Chen and L. H. Lee, "Rigorous generation of digital orthophotos from SPOT images," *Photogramm. Eng. Remote Sens.*, vol. 59, no. 5, pp. 655–661, 1993.

[8] T. Toutin, "Block bundle adjustment of IKONOS in-track image," *Int. J. Remote Sens.*, vol. 24, no. 4, pp. 851–857, 2003.

[9] A. Habib, S. W. Shin, K. Kim, C. Kim, K. I. Bang, E. M. Kim, and D. C. Lee, "Comprehensive analysis of sensor modeling alternatives for high resolution imaging satellites," *Photogramm. Eng. Remote Sens.*, vol. 73, no. 11, pp. 1241–1251, Nov. 2007.

[10] T. Kim, H. Kim, and S. Rhee, "Investigation of physical sensor models for modeling SPOT 3 orbits," *Photogramm. Rec.*, vol. 22, no. 119, pp. 257–273, Sep. 2007.

[11] L. C. Chen and L. Y. Chang, "Three dimensional positioning using SPOT stereostrips with sparse control," *J. Surveying Eng.*, vol. 124, no. 2, pp. 63–72, May 1998.

[12] N. Yastikli and K. Jacobsen, "Influence of system calibration on direct sensor orientation," *Photogramm. Eng. Remote Sens.*, vol. 71, no. 5, pp. 629–633, May 2005.

[13] T. Weser, F. Rottensteiner, J. Willneff, J. Poon, and C. S. Fraser, "Development and testing of a generic sensor model for pushbroom satellite imagery," *Photogramm. Rec.*, vol. 23, no. 123, pp. 255–274, Sep. 2008.

[14] T. Toutin, "Spatiotriangulation with multisensory HR stereo-images," *IEEE Tran. Geosci. Remote Sens.*, vol. 44, no. 2, pp. 456–462, Feb. 2006.

[15] F. Rottensteiner, T. Weser, A. Lewis, and C. S. Fraser, "A strip adjustment approach for precise georeferencing of ALOS optical imagery," *IEEE Tran. Geosci. Remote Sens.*, vol. 47, no. 12, pp. 4083–4091, Dec. 2009.

[16] E. M. Mikhail and J. S. Bethel, *Introduction to Modern Photogrammetry*. New York: Wiley, 2001, pp. 446–454.

[17] T. A. Teo, L. C. Chen, C. L. Liu, Y. C. Tung, and W. Y. Wu, "DEM-aided block adjustment for satellite images with weak convergence geometry," *IEEE Trans. Geosci. Remote Sens.*, vol. 48, no. 4, pp. 1907–1918, Apr. 2010.

[18] C. V. Tao and Y. Hu, "A comprehensive study of the rational function model for photogrammetric processing," *Photogramm. Eng. Remote Sens.*, vol. 67, no. 12, pp. 1347–1357, Dec. 2001.

[19] H. G. Sohn, C. H. Park, and H. Chang, "Rational function model-based image matching for digital elevation models," *Photogramm. Rec.*, vol. 20, no. 112, pp. 366–383, Dec. 2005.

[20] E. M. Mikhail and F. Ackermann, *Observation and Least Squares*. Washington, DC: Univ. Press America, 1982.

[21] J. C. McGlone, E. M. Mikhail, J. Bethel, and R. Mullen, *Manual of Photogrammetry,* 5th ed. Bethesda, MD: ASPRS, 2004, pp. 847–887.

Liang-Chien Chen received the M.S.E. degree from the National Cheng Kung University (NCKU), Tainan, Taiwan, in 1974 and the Ph.D. degree from the University of Illinois, Urbana, in 1985.

From 1985 to 1986, he was with the Institute of Photogrammetry, NCKU. Since 1986, he has been a Professor with the Center for Space and Remote Sensing Research, National Central University, Jhongli City, Taiwan. He is in charge of the Digital Photogrammetry Laboratory and the Earth Resource Satellite Ground Receiving Station. His research activities are focused on the domain of digital photogrammetry, geometrical data processing for remotely sensed data, image feature extraction, lidar processing, and terrain analysis.

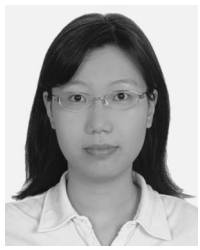

Wen-Chi Chang received the B.S. and M.S.E. degrees in civil engineering from the National Central University, Jhongli City, Taiwan, in 2008 and 2009, respectively, where she is currently working toward the Ph.D. degree in the Department of Civil Engineering.

In 2009, she joined the Digital Photogrammetry Laboratory, Center for Space and Remote Sensing Research, National Central University, as a Research Assistant.

Tee-Ann Teo received the M.S.E. and Ph.D. degrees from the National Central University, Jhongli City, Taiwan, in 2002 and 2008, respectively.

He was with the Center for Space and Remote Sensing Research, National Central University, as a Postdoctoral Research Fellow in 2008. He is currently an Assistant Professor with the Department of Civil Engineering, National Chiao Tung University, Hsinchu, Taiwan. His research activities are focused on cyber city modeling, geometrical data processing for remotely sensed data, and lidar processing.